Front. Struct. Civ. Eng. 2024, 18(7): 1015–1027
https://doi.org/10.1007/s11709-024-1063-5

RESEARCH ARTICLE

Stress–strain relationship for reactive powder concrete with recycled powder under uniaxial compression

Peng ZHU[a,b], Yunming ZHU[a], Wenjun QU[a], Liyu XIE[a*]

[a] *College of Civil Engineering, Tongji University, Shanghai 200092, China*

[b] *Key Laboratory of Performance Evolution and Control for Engineering Structures of Ministry of Education, Tongji University, Shanghai 200092, China*

[*] *Corresponding author. E-mail: liyuxie@tongji.edu.cn*

ABSTRACT The recycled powder (RP) from construction wastes can be used to partially replace cement in the preparation of reactive powder concrete. In this paper, reactive powder concrete mixtures with RP partially replacing cement, and natural sand instead of quartz, are developed. Standard curing is used, instead of steam curing that is normally requested by standard for reactive powder concrete. The influences of RP replacement ratio (0%, 10%, 20%, 30%), silica fume proportion (10%, 15%, 20%), and steel fiber proportion (0%, 1%, 2%) are investigated. The effects of RP, silica fume, and steel fiber proportion on compressive strength, elastic modulus, and relative absorption energy are analyzed, and theoretical models for compressive strength, elastic modulus, and relative absorption energy are established. A constitutive model for the uniaxial compressive stress–strain relationship of reactive powder concrete with RP is developed. With the increase of RP replacement ratio from 0% to 30%, the compressive strength decreases by 42% and elastic modulus decreases by 24%.

KEYWORDS recycled powder, reactive powder concrete, elastic modulus, relative absorbed energy, stress–strain relationship

1 Introduction

Reactive powder concrete (RPC) is a type of ultra-high-performance concrete (UHPC). Steel fiber can be added to improve its toughness, and coarse aggregates can be removed [1]. A compact microstructure can be formed by optimizing the particle filling of the constituent components in the mixture design, which gives RPC extremely high strength and outstanding durability [2].

The amount of global construction waste is huge, with 2.3 billion tons generated annually in China and more than 800 million tons in the European Union [3]. The traditional landfill method used for disposal causes environmental pollution and demands land. Recycled powder (RP), which typically has particles smaller than 0.16 mm [4], is the fine powder made from construction waste, such as leftover concrete and clay bricks. Considering its pozzolanic activity, RP can be used as an additive to substitute cement in RPC [5] to reduce the proportion of cement and also reduce environmental pollution. Generally, the concrete strength steadily reduces as the RP replacement ratio increases [6–10], due to RP's lower hydration activity than that of cement. Some other studies have found that RP replacement ratio of 30% can increase the strength of concrete [11,12], probably because RP can improve the pore structure, while the particles of RP can play a role of crystal nuclei, which promotes the C-S-H formation [13]. Zhu et al. [14] have designed the optimal mix proportion by an improved method based on the Dinger−Funk equation and have experimentally investigated the mechanical properties of RP concrete.

For UHPC, the uniaxial compressive stress–strain curve has been previously studied. Graybeal [15] investigated curing method on the ascending section for the ultra-high-performance fiber-reinforced concrete (UHPFRC), and derived the prediction equations for strength increase with time. Steel fiber can considerably boost the strength,

Article history: Received Feb 3, 2023; Accepted Aug 31, 2023

ductility, and stiffness of RPC, according to Bae et al. [16]. They also suggested a stress–strain model based on the Collins model [17] with the elastic modulus as the main variable. However, this model had poor prediction accuracy of test results. Ji et al. [18] fitted multiple test curves into a single curve. The polynomial form was chosen for the ascending section in the curve, and its applicability was limited. Also, due to the limitation of test conditions, a large dispersion in the descending section of test curves was observed. Zhang et al. [19] established a stress−strain model for UHPFRC based on modified Kent−Park model. The descending section model consisted of two straight lines, making it difficult to accurately characterize the actual stress-strain relationship. Hashim et al. [20] considered the impact of fiber types on the whole curve and obtained polynomial equations for the uniaxial compressive stress–strain curve. Tang et al. [21] studied the constitutive relationship of aluminate UHPC with steel fibers at different temperatures. In addition, different models for RPC have been proposed in accordance with codes of different nations, and the model curves mostly consist of two or three straight lines, which cannot accurately reflect the stress–strain relationship, resulting in a waste of materials.

Study of the constitutive relationship of RPC is still limited, and there is no research on that of reactive powder concrete with recycled powder (RPRPC). Studying the mechanical properties and constitutive relationship of RPRPC can provide reference for the formulation of relevant standards and can contribute to industrial production and application. The effects of RP, silica fume, and steel fiber proportions are studied by experiments in this work. Theoretical models for compressive strength, elastic modulus, relative absorption energy, and also the whole uniaxial compressive stress–strain curve of RPRPC, are developed.

2 Experiment preparation

2.1 Materials

Chemical properties of RP are listed in Table 1. The average particle size in this work was 16.163 μm. P.O 42.5 Portland cement was used.

Copper-plated hook-end steel fibers were selected with a length of 13 mm, aspect ratio of 60, elastic modulus of 200 GPa, and tensile strength of 2850 MPa. A polycarboxylate superplasticizer with 41% solid content and 31.8% water reduction rate was used.

2.2 Mixture proportion

A proportion design method suitable for RPRPC was developed according to the Dinger−Funk model, based on work by Zhu et al. [14], and the mixture ratio for the experiment was created accordingly as shown in Table 2. The effect of RP was studied, and ratios of cement replacement by RP were 0%, 10%, 20%, and 30%, as Group A. Silica fume was investigated, and the mass ratios of silica fume to cement and RP were 10%, 15%, and 20%, as Group B. The volume fractions of steel fiber were 0%, 1%, 1.5%, and 2%, as Group C.

2.3 Specimen preparation

Three cylindrical specimens of Φ100 mm (diameter) × 200 mm (height) were made for each mixture, with a total of 27 specimens.

After mixing the cement, silica fume, and RP for 2 min, 2/3 of the water and water reducing agent were added and mixed for 3 min. All the natural sand was added and mixed for 3 min, and then the remaining 1/3 of the water and water reducing agent for 6 min. As steel fibers were used, an additional 3–6 min of mixing was required.

The specimens were kept in the laboratory environment of (20 ± 5) °C for 48 h and then demolded. After demolding, they were placed in a standard curing room with a temperature of (20 ± 2) °C and humidity of more than 90% for 28 d.

2.4 Test methods

A rigid testing machine with MTS815.02 electro-hydraulic servo test system was used. The specimen undergoes longitudinal deformation along the direction of loading and also transverse expansion according to Poisson's ratio effect in the uniaxial compression test. Thus, friction is generated between the pressure plate and the concrete specimen. To eliminate its effect on the tests, two layers of Teflon films were used on the specimen. To acquire the additional deformation due to the friction layers and the machine, a steel cylinder of the same size as the specimen was examined. The true deformation of the specimen was the measured total displacement of the loading cylinder minus the additional longitudinal deformation.

Table 1 Chemical properties of RP used in this study

Material	Chemical composition							
	Na_2O (%)	MgO (%)	Al_2O_3 (%)	SiO_2 (%)	SO_3 (%)	K_2O (%)	CaO (%)	Fe_2O_3 (%)
RP	0.84	2.17	11.70	46.90	1.49	2.30	19.30	5.62

Table 2 Concrete Mixture masses per cubic meter of mix

No.	Water binder ratio	Cement (kg)	RP (kg)	Silica fume (kg)	Natural sand (kg)	Super plasticizer (kg)	Water (kg)	Steel fiber (vol%)
A1	0.16	1000	0	150	1000	28.75	166.75	0
A2	0.16	900	100	150	1000	28.75	166.75	0
A3	0.16	800	200	150	1000	28.75	166.75	0
A4 (B2, C1)	0.16	700	300	150	1000	28.75	166.75	0
B1	0.16	700	300	100	1000	27.50	159.50	0
B3	0.16	700	300	200	1000	30.00	174.00	0
C2	0.16	700	300	150	1000	28.75	166.75	1
C3	0.16	700	300	150	1000	28.75	166.75	1.5
C4	0.16	700	300	150	1000	28.75	166.75	2

Note: The ratio of solid content in water-reducing agents to the amount of cementitious material was 1%.

3 Results and discussion

3.1 Failure modes

The typical failure modes of specimens were selected (Fig. 1). Comparing A1 (mass substitution ratio of RP R_{rp} = 0%) with A4 (R_{rp} = 30%), it can be found that RP had little effect on the failure mode. Comparing A4 (B2) (mass substitution ratio of silica fume R_{sf} = 15%) with B3 (R_{sf} = 20%), it can be seen that the silica fume had little effect on the failure mode. Small cracks formed and fragments began to break off as the pressure approached the peak load. As loading continued, the crack width increased and some all-through cracks developed in the specimens, leading to the splitting and collapse of the specimens. Obvious brittle failure was observed for all specimens without steel fibers.

For specimens with steel fibers, no all-through cracks developed; the crack lengths were within 2/3 of the specimen height. Steel fibers under tension could be observed from the crack opening. Steel fibers clearly played an important part in limiting fracture formation.

3.2 Compressive strength

The compressive strength dropped as the RP replacement ratio rose, as indicated in Fig. 2(a). With the increase of RP replacement ratio from 0% to 10%, 20%, and 30%, the compressive strength decreased by 22%, 31%, and 42%, due to RP having a lower hydration activity than cement [22].

Figure 2(b) shows that as silica fume increased from 10% to 15% and 25%, the compressive strength increased by 20% and 48%, due to the pozzolanic activity in the ternary cementitious system and also the micro filling effect. This is in agreement with the results by Ahmed et al. [23] and Park et al. [24].

Figure 2(c) shows that with the chosen increments of steel fiber proportion from 0% to 1%, 1.5%, and 2%, the compressive strength increased by 18%, 24%, and 65%. The stress between the steel fiber and the matrix decreases as the amount of steel fiber increases, which delays the formation and expansion of cracks and finally increases the strength [25].

(a) (b) (c) (d)

Fig. 1 Failure modes of concrete: (a) specimen A1 (R_{rp} = 0%); (b) specimen A4 (R_{rp} = 30%, R_{sf} = 15%); (c) specimen B3 (R_{sf} = 20%); (d) specimen C4 (V_{sf} = 2%).

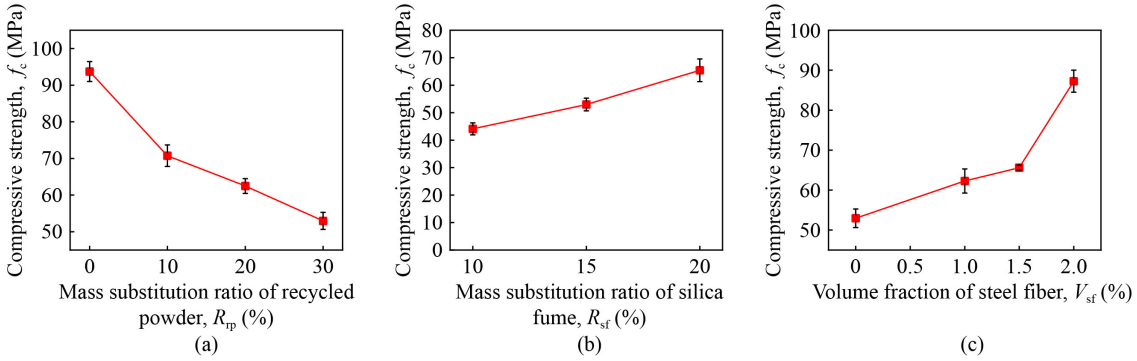

Fig. 2 Compressive strength versus proportions of: (a) RP; (b) silica fume; (c) steel fibers.

3.3 Elastic modulus

Figure 3(a) shows that the elastic modulus decreased by 5%, 13%, and 24% when the RP replacement ratio increased from 0% to 10%, 20%, and 30%. There was a significantly lower value of the elastic modulus at the RP replacement ratio value of 30%, which is consistent with the results by Tang et al. [13]. The compressive strength dropped as the RP replacement ratio rose, which is in line with the idea that the elastic modulus and compressive strength of concrete are positively associated. In Fig. 3(b), the elastic modulus decreased by 7% with the increase of silica fume amount from 10% to 15%, while there was negligible decrease of elastic modulus as silica fume amount increased from 15% to 20%. In Fig. 3(c), the elastic modulus increased by 35%, 25%, and 43%, when the volume proportion of steel fiber increased from 0% to 1%, 1.5%, and 2%. The elastic modulus increased with the increase of steel fiber proportion in general, which is consistent with previous studies [26]. The steel fiber can increase the stiffness significantly.

3.4 Energy absorption capacity

The relative absorbed energy U_r can characterize the energy absorption capacity of concrete, as Eq. (1).

$$U_r = \frac{\int_0^{\varepsilon_0} \sigma(\varepsilon)\,\mathrm{d}\varepsilon}{f_c \varepsilon_0}, \tag{1}$$

where f_c is the compressive strength and ε_0 is the peak strain.

The relative absorbed energy is within the range of 0.5–1, and the closer it is to 0.5, the closer the material is to linear elastic behavior. The ascending curves of Groups A and C were normalized and averaged, as shown in Fig. 4(a), and the relative absorbed energy was calculated according to these ascending curves. Figures 4(b) and 4(c) show variations in relative absorbed material for different mixes. When the RP replacement ratio increased from 0% to 10%, 20%, and 30%, the relative absorbed energy increased by 2%, 4%, and 7% which was close to a linear relationship. The relative absorbed energy decreased by 2% and 7%, respectively, when the steel fiber content increased from 1% to 1.5%, and 2%. According to the study [27], compressive strength correlates negatively with relative absorbed energy and favorably correlated with brittleness.

For fiber concrete, the method in ASTM-C1018 [28] combines the energy ratio method with the characteristic point method to characterize the bending toughness, and is widely used. The method in CECS13:89 specification [29] defines a compression toughness characterization method based on ASTM-C1018, and assumes the stress corresponding to the initial cracking point is 0.85 times the peak stress, which makes its application easier. The compressive toughness index $\eta_{c,5}$ is defined as Eq. (2):

$$\eta_{c,5} = \frac{S_{OACD}}{S_{OAB}}. \tag{2}$$

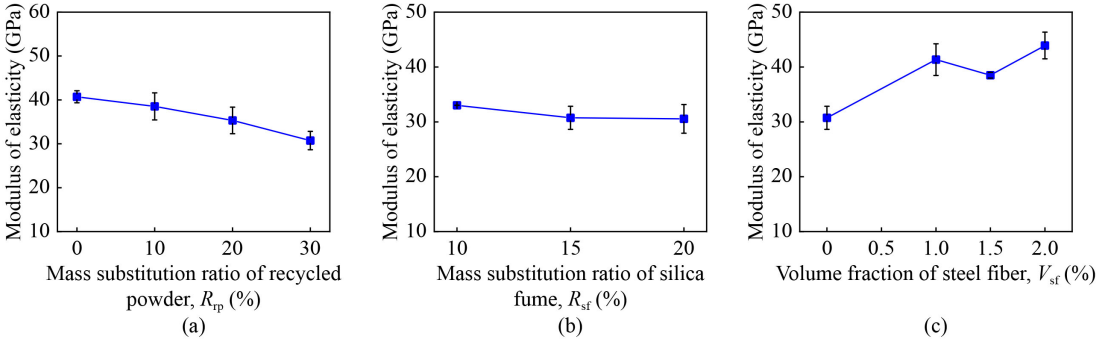

Fig. 3 Elastic modulus versus proportion of: (a) RP; (b) silica fume; (c) steel fiber.

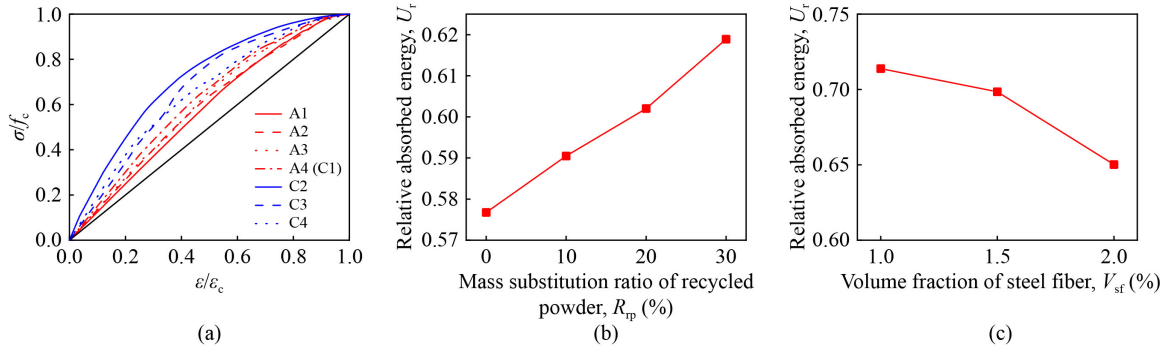

Fig. 4 Relative absorbed energy: (a) normalized curves for ascending section; (b) U_r versus R_{rp}; (c) U_r versus V_{sf}.

Points A to D are marked in Fig. 5. Point A is the assumed concrete initial cracking point. S_{OACD} and S_{OAB} are the areas under the curve to Points C and A, respectively.

The compressive toughness index $\eta_{c,5}$ of concrete mixtures with steel fibers was calculated, and the results are shown in Fig. 6. When the steel fiber proportion was 0%, 1.0%, 1.5%, and 2.0%, $\eta_{c,5}$ had values of 4.16, 4.45, 4.71, and 4.26, respectively. When the steel fiber proportion increased from 0% to 1% and 1.5%, the compressive toughness index increased by 7.0% and 13.2%, respectively, showing that the steel fiber can improve the ductility of the concrete. However, when it increased from 1.5% to 2%, the compressive toughness index reduced slightly (but remained higher than the initial value), indicating there is an upper limit for the proportion of steel fibers in increasing the energy absorption capacity. A large proportion of steel fibers can result in the fiber clustering, which can affect the ability to resist cracking.

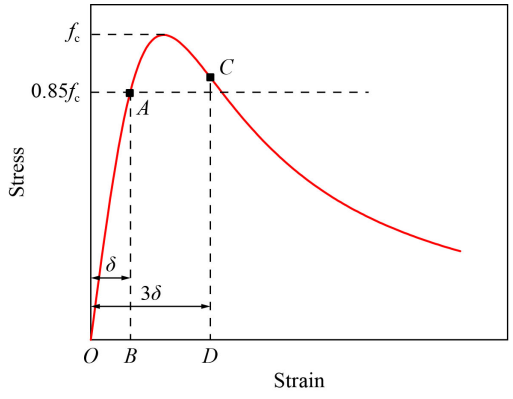

Fig. 5 Characteristics of the curve for the calculation of compressive toughness index.

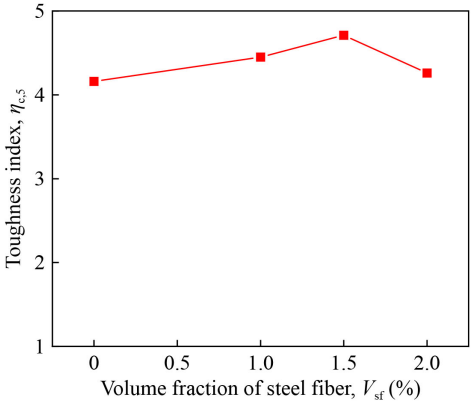

Fig. 6 Compression toughness index versus steel fiber proportion.

4 Model development

4.1 Model of compressive strength

For RPRPC without steel fibers, the relationship of the compressive strength with RP replacement ratio was developed by regression analysis, as Eq. (3). The influence of steel fibers was further considered, and Eq. (4) was developed.

$$f_{c,rp} = -6.54R_{rp}^{0.53} + 93.68,\ (R^2 = 0.95) \tag{3}$$

$$f_{c,rpsf} = f_{c,rp}\left(1 + 0.1V_{sf}^{2.8}\right),\ (R^2 = 0.83) \tag{4}$$

where R_{rp} is the RP replacement ratio, $f_{c,rp}$ is the compressive strength of RPRPC without steel fiber, and $f_{c,rpsf}$ is the compressive strength of RPRPC with steel fiber.

4.2 Model of elastic modulus

As indicated in Fig. 7, data from prior studies [9,30–33] were collected and summarized with the experimental results from this investigation. The specimen shapes and sizes used were different in different literatures. The cross-sectional shape and size of the specimen has negligible effect on the elastic modulus [34–36], whereas the size has a considerable impact on compressive strength. For cylindrical specimens of different sizes, compressive strength was converted to that of Φ150 mm × 300 mm specimens based on the specimen height/diameter ratio according to ASTM C49/C49M-21 [37]. For cubic specimens, the compressive strength was

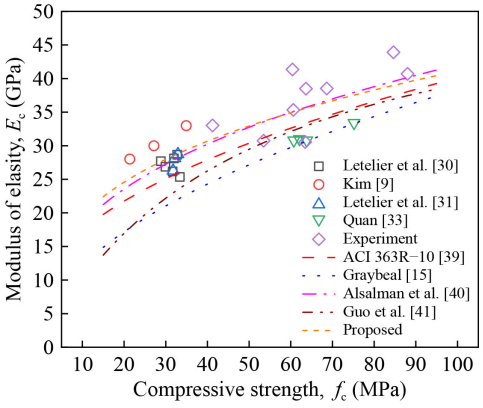

Fig. 7 Elastic modulus versus compressive strength.

converted to that of Φ150 mm × 300 mm cylindrical specimens according to the method by UNESCO [38]. The compressive strength−elastic modulus relationship was developed by regression analysis as Eq. (5). Different models including the ones for high performance concrete (HPC) and UHPC are summarized and compared in Table 3, and Fig. 7. The model established in this study shows the best fit, and the Alsalman model is also good. The ACI 363R-10, Graybeal, and Guo models have small R^2 values and also underestimated the elastic modulus.

$$E_c = 9.42 f_c^{0.32}. \ (R^2 = 0.64) \tag{5}$$

Table 3 Elastic modulus-compressive strength relationship

Ref.	Relationship models	f_c (MPa)	R^2
ACI 363R-10 [39]	$E_c = 3.32\sqrt{f_c} + 6.9$	[21,83]	0.47
Graybeal [15]	$E_c = 3.84\sqrt{f_c}$	[25,193]	−0.55
Alsalman et al. [40]	$E_c = 8.01 f_c^{0.36}$	[31,235]	0.63
Guo et al. [41]	$E_c = \left(0.0172 + \frac{0.8364}{f_c}\right)^{-1}$	[60,220]	−0.03
This paper	$E_c = 9.42 f_c^{0.32}$	[15,95]	0.64

4.3 Model of relative absorbed energy

Results for the relationship between the relative absorbed energy with compressive strength are shown in Fig. 8. For both Groups A and C, the relative absorbed energy decreased with the increase of compressive strength. Furthermore, the relative absorbed energy of Group C specimens was significantly greater than that of Group A specimens with similar compressive strength, which indicated that steel fibers can increase the relative absorbed energy. Models for the relative absorbed energy of RPRPC without steel fibers and with steel fibers were developed by regression analysis as Eqs. (6) and (7), respectively.

$$U_{r,rp} = f_c^{-0.12}, \ (R^2 = 0.84) \tag{6}$$

$$U_{r,rpsf} = 2.16 f_c^{-0.27}, \ (R^2 = 0.98) \tag{7}$$

where $U_{r,rp}$ is the relative absorbed energy of RPRPC without steel fibers, and $U_{r,rpsf}$ is the relative absorbed energy of RPRPC with steel fibers.

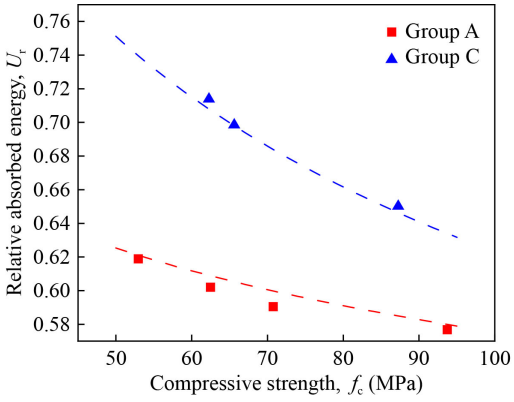

Fig. 8 Relative absorbed energy versus compressive strength.

4.4 Model of stress–strain curve

The stress–strain curve consists of the ascending section and the descending section. The typical models are summarized in Table 4. NSC is normal strength concrete, and SFRC is steel fiber reinforced concrete. There have been many studies on the stress–strain constitutive relationship of NSC, and some whole-curve constitutive models have been proposed, typically the Carreira–Chu model [42], the Guo model [43], the CEB-FIP-1990 model [44], and the GB50010-2010 model [45]. These four models are chosen as the reference models. The Carreira–Chu model is the most widely used due to its simplicity, and many scholars have applied this model to different concrete materials, such as UHPC, confined concrete, and self-compacting concrete, by modifying the value of parameter n or adding new parameters [46]. The other three models are also widely used and have been used in the development of specifications in various countries.

All the models were compared with the experimental curves, as shown in Figs. 9 and 10. The ascending and descending sections of the curves, which are the sections before and after the peaks, were studied separately.

In Table 4, E_{ci} is the secant modulus at the peak stress; ε_c is the peak strain; $\varepsilon_{c,lim}$ is the ultimate strain.

$$x = \frac{\varepsilon}{\varepsilon_c}, \ y = \frac{\sigma}{f_c}, \ RI = \frac{V_f l_f}{d_f}, \tag{8}$$

where V_f is the volume proportion of steel fibers, l_f is the length of steel fiber (mm), and d_f is the diameter of steel fiber (mm).

4.4.1 Model of ascending section

All 11 models in Table 4 were compared with results for

Table 4 Theoretical stress–strain models of NSC, UHPC, and SFRC

Concrete type	Ref.	Model	Parameters
NSC	Carreira and Chu [42]	$y=\dfrac{nx}{n-1+x^n}$	$n=\dfrac{1}{1-\dfrac{f_c}{\varepsilon_c E_{it}}}$
	Guo [43]	$y=\begin{cases}(\alpha_a-2)x^3+(3-2\alpha_a)x^2+\alpha_a x, & (0<x\leqslant 1)\\ \dfrac{x}{\alpha_d(x-1)^2+x}, & (x>1)\end{cases}$	$\alpha_a=2.4-0.0125f_c$ $\alpha_d=0.157f_c^{0.785}-0.905$
	CEB-FIP-1990 [44]	$q=\dfrac{\varepsilon_{c,lim}}{\varepsilon_c},\ t=\dfrac{E_{ci}}{E_{c1}}$ $y=\begin{cases}\dfrac{tx-x^2}{1+(t-2)x}, & (0<x\leqslant q)\\ \dfrac{1}{\left(\dfrac{\xi}{q}-\dfrac{2}{q^2}\right)x^2+\left(\dfrac{4}{q}-\xi\right)x}, & (x>q)\end{cases}$	$q=\dfrac{1}{4}\left[t+2+\sqrt{(t+2)^2-8}\right]$ $\xi=\dfrac{4\left[q^2(t-2)+2q-t\right]}{(q(t-2)+1)^2}$
	GB50010-2010 [45]	$\sigma=(1-d_c)E_c\varepsilon$ $d_c=\begin{cases}1-\dfrac{\rho_c n}{n-1+x^n}, & (x\leqslant 1)\\ 1-\dfrac{\rho_c^*}{\alpha_c(x-1)^2+x}, & (x>1)\end{cases}$	$\rho_c=\dfrac{f_c}{E_c\varepsilon_c}$ $n=\dfrac{E_c\varepsilon_c}{E_c\varepsilon_c-f_c}$ $\alpha_c=0.157f_c^{0.785}-0.905$
UHPC	Collins et al. [17]	$y=\dfrac{nx}{n-1+x^{nk}}$	$n=0.8+\dfrac{f_c}{17}$ $k=0.67+\dfrac{f_c}{62}$
	Wu [47]	$y=\begin{cases}(4A-5)x^6+(6-5A)x^5+Ax, & (0\leqslant x\leqslant 1)\\ \dfrac{x}{\alpha(x-1)^2+x}, & (x>1)\end{cases}$	$A=1.1,\ \alpha=3$
	Wee et al. [48]	$y=\begin{cases}\dfrac{nx}{n-1+x^n}\\ \dfrac{k_1 nx}{k_1 n-1+x^{k_2 n}}\end{cases}$	$n=\dfrac{1}{1-\dfrac{f_c}{\varepsilon_c E_{it}}}$ $k_1=\left(\dfrac{50}{f_c}\right)^3,\ k_2=\left(\dfrac{50}{f_c}\right)^{1.3}$
SFRC	Prabha et al. [49]	$y=\dfrac{nx}{n-1+x^{nk}}$	$n=\dfrac{1}{1-\dfrac{f_c}{\varepsilon_c E_{it}}}$ $k=0.75-0.075RI$
	Lv et al. [50]	$\sigma=(1-d_c)E_c\varepsilon$ $d_c=\begin{cases}1-\dfrac{\rho_c n}{n-1+x^n}, & (x\leqslant 1)\\ 1-\dfrac{\rho_c n}{\alpha_c(x-1)^2+x}, & (x>1)\end{cases}$	$\alpha_c=(0.157f_c^{0.785}-0.905)(1-0.00192\dfrac{l_f}{d_f}V_f^{0.08})$
	Ding et al. [51]	$y=\begin{cases}\dfrac{nx}{n-1+x^n}, & (0<x\leqslant 1)\\ \dfrac{x}{\alpha_c(x-1)^2+x}, & x>1\end{cases}$	$n=\dfrac{1}{1-\dfrac{f_c}{\varepsilon_c E_c}}$ $\alpha_c=0.13\times(1+RI)(0.157f_c^{0.785}-0.905)$
	Lee et al. [52]	$y=\dfrac{Ax}{A-1+x^B}$	$A=B=\dfrac{1}{1-\dfrac{f_c}{\varepsilon_c E_c}},\quad (0\leqslant x\leqslant 1)$ $A=1+0.723RI^{-0.957},\quad (x>1)$ $B=\left(\dfrac{f_c}{50}\right)^{0.064}\left(1+0.882RI^{-0.882}\right)\geqslant A,\quad (x>1)$

Groups A and C. Considering the ascending section (section before the peak), models in Table 4 are divided into two groups, and the ascending sections of models in the same group are the same. The Carreira–Chu model and Wee model are in one group, while the GB50010-2010 model, Lv model, Ding model, and Lee model are in the other group. For the ascending section, the difference between these two groups of models was small. The initial tangent modulus was used in the Carreira–Chu model, and the elastic modulus was used in the GB50010-2010 model. This variation in modulus is the only difference between these two groups of models. Also, the Carreira–Chu model and the GB50010-2010 model are used to represent these two groups of models. Both the R-squared (R^2) and root-mean squared error ($RMSE$) were calculated.

The results of R^2 were shown in Table 5, and all 11 models had R^2 values above 0.75. For all the specimens,

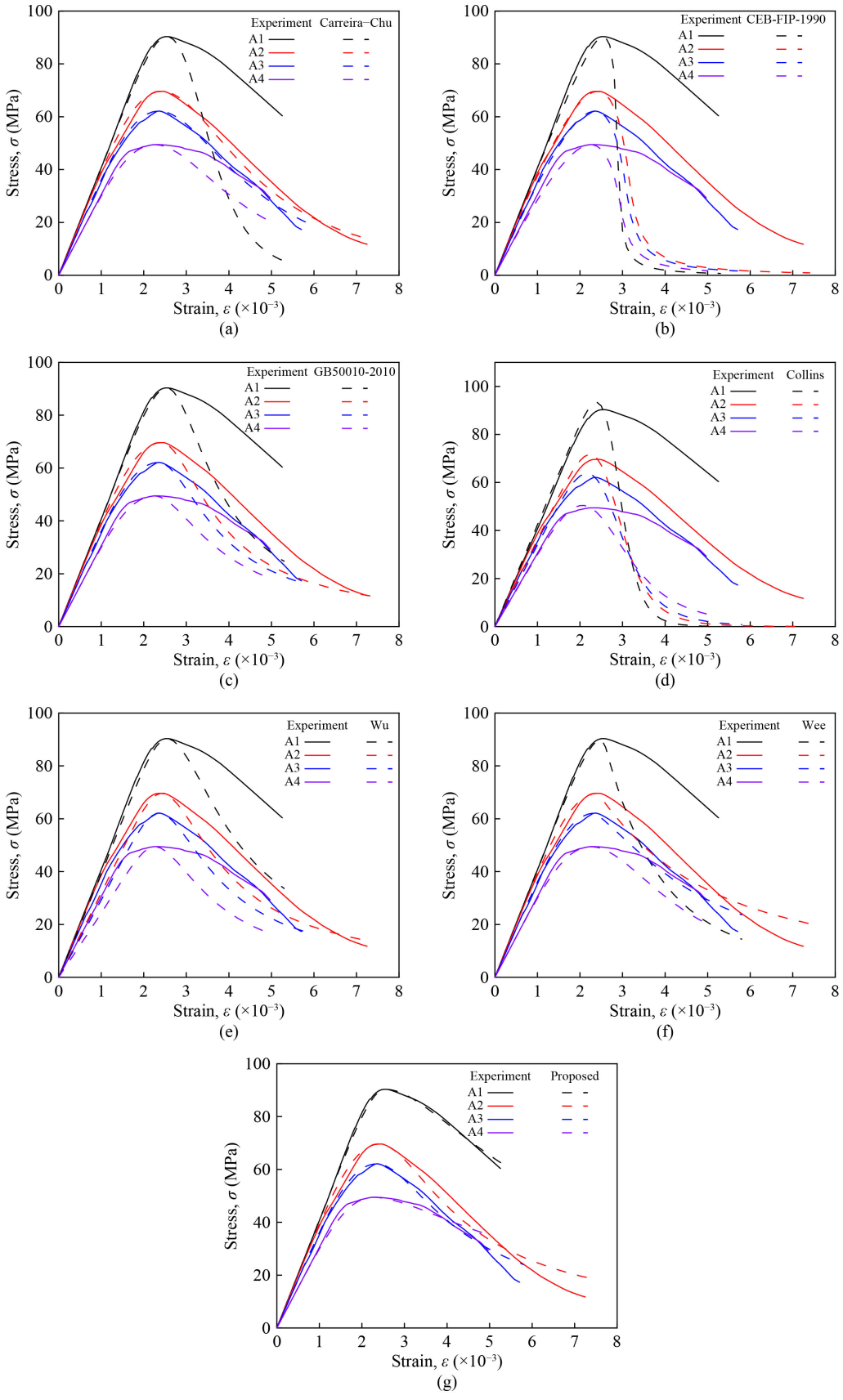

Fig. 9 Theoretical and experimental curves for Group A: (a) Carreira–Chu model; (b) CEB-FIP-1990 model; (c) GB50010-2010 model; (d) Collins model; (e) Wu model; (f) Wee model; (g) proposed model.

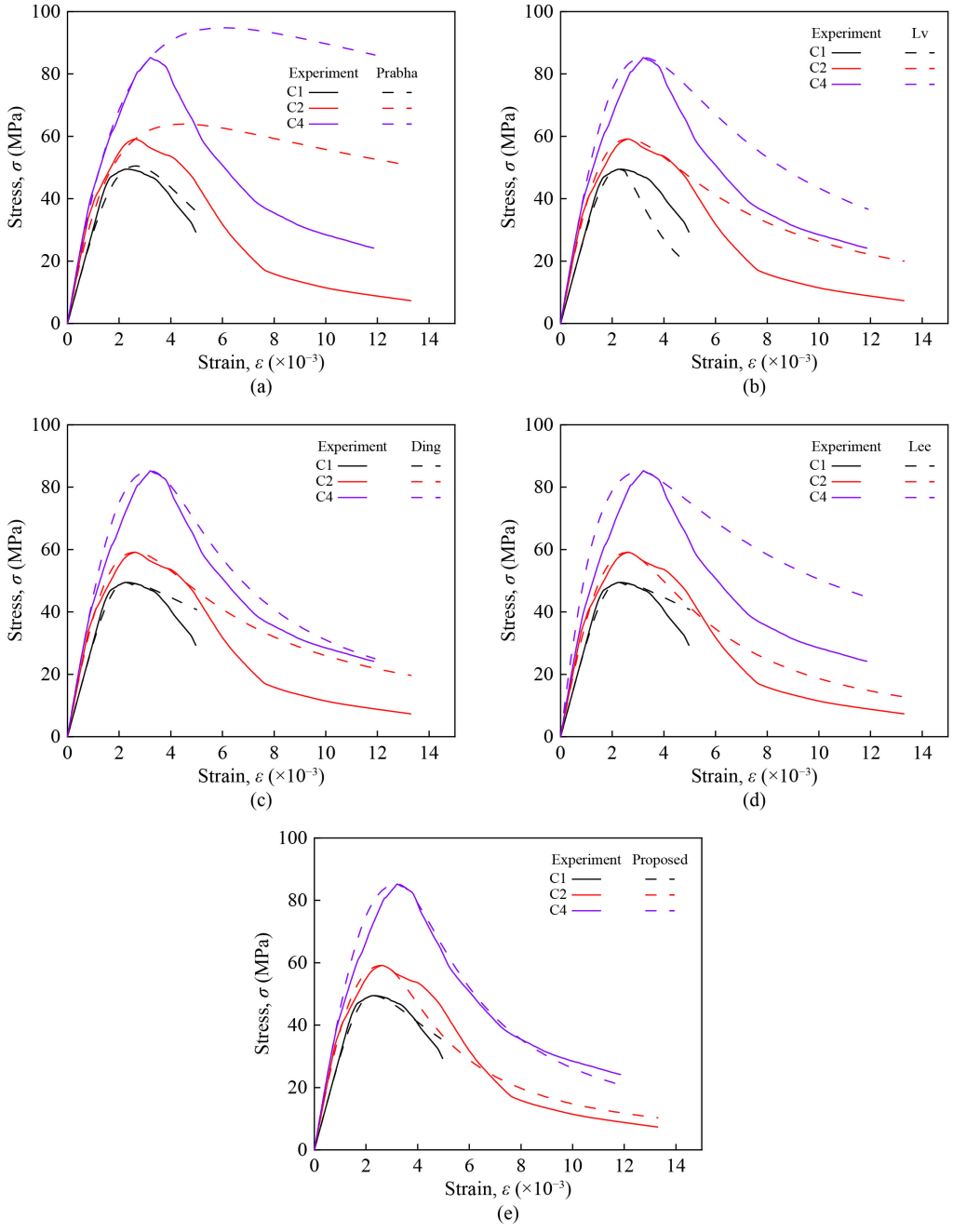

Fig. 10 Theoretical and experimental curves for Group C: (a) Prabha model; (b) Lv model; (c) Ding model; (d) Lee model; (e) Proposed model.

Table 5 R^2 of models for ascending section

Model	A1	A2	A3	A4	C2	C4	Average
Carreira–Chu	0.999	0.994	0.998	0.995	0.991	0.962	0.990
Guo	0.974	0.988	0.988	0.988	0.975	0.977	0.982
GB50010-2010	0.999	0.995	0.998	0.995	0.991	0.965	0.991
CEB-FIP-1990	0.996	0.999	0.998	0.981	0.990	0.988	0.992
Collins	0.995	0.990	0.990	0.997	0.906	0.928	0.968
Wu	0.996	0.962	0.951	0.908	0.757	0.875	0.908
Prabha	0.998	0.999	0.999	0.985	0.988	0.998	0.995

the R^2 values of most models exceeded 0.9. The Wu model performed relatively poorly in Group C. The results of *RMSE* were compared, as shown in Fig. 11. The Wu model had the largest *RMSE* values in most cases. Although the Prabha model had the smallest average *RMSE* value, it is not suitable as a basis for modeling because it does not ensure the derivative is zero at the peak point. The Carreira–Chu, GB50010-2010, and CEB-FIP model gave smaller *RMSE* values, and the Carreira–Chu model was suggested as the model for the ascending part, as per Eqs. (9) and (10), considering its simplicity.

$$y = \frac{nx}{n-1+x^n},\ (x<1) \tag{9}$$

$$n = \frac{1}{1-\dfrac{f_c}{\varepsilon_c E_{it}}}. \tag{10}$$

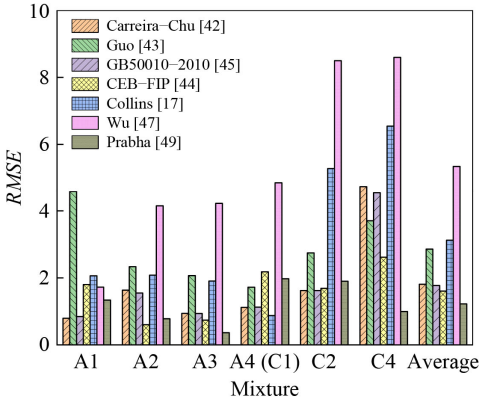

Fig. 11 RMSE of different models for the ascending section.

4.4.2 Model of descending section

The descending section (section after the peak) of the curves is the focus of the study on concrete constitutive model. Owing to the significant influence of steel fiber on the descending section, a prediction model for the descending section of RPRPC without steel fiber was established first, and the impact of steel fibers was further considered.

Three widely used concrete models (Carreira–Chu, GB50010-2010, and CEB-FIP-1990) were selected for the RPRPC without steel fibers, as shown in Fig. 9.

The deviation of the Carreira–Chu model prediction for specimens A1 is significant, as no RP was used in A1 and it had relatively higher strength. This model is not suitable for high-strength concrete. When the concrete strength exceeds the applicability range of this model, the increase of parameter n will excessively increase x^n, which will excessively change the shape of the descending section and make it deviate from the test curve.

The descending sections of all the prediction curves by the CEB-FIP-1990 model have significantly higher descending gradients than test curves and could not characterize the ductility of concrete. This model showed a similar problem in previous studies. For example, Nematzadeh et al. [53] compared this model with the test curve of Wang et al. [54], and it was found that the descending section described by this model was too steep. The possible reason may be that the range of parameters for the descending section in the CEB-FIP-1990 model is not restricted.

In addition to the above three models, typical UHPC models were also selected for comparison with the experimental curves.

Based on the Carreira–Chu model, the Collins model, a typical model for UHPC, added the parameter k to correct the descending speed of the curve and proposed the relationship between parameters n, k, and f_c. But the values of parameters n, k were obviously too large for the present experimental data, resulting in curves, predicted by the model for specimens A1 and A2, with relatively higher compressive strength, have descending gradients that were too large.

The Guo model was used as the foundation for the Wu model. The relationship between the shape parameter α and the peak stress of the descending section is not established, and the constant value of α leads to a constant descending rate of the curve, which reduces the applicability of the model. Additionally, the experimental data in this research do not support the Wu model.

Based on the Carreira–Chu model, the Wee model also introduced a parameter k_1, and the shape of the descending curve has a connection to the parameters n, k_1, and k_2. In this study, it agreed well with the test curves of the mixtures with relatively lower strength, but the predicted curve of the descending section was much steeper than in the case of the test curve of the mixture with high strength (A1).

Following the analysis mentioned above, the descending section of stress–strain model for RPRPC without steel fiber is proposed as following:

$$y = \frac{x}{\alpha_c (x-1)^2 + x},\ (x>1) \tag{11}$$

$$\alpha_{c0} = 0.157 f_c^{0.785} - 0.905, \tag{12}$$

$$\varphi_{rp} = -18R_{rp}^2 + 5.63R_{rp} + 0.18, \tag{13}$$

$$\alpha_c = \varphi_{rp}\alpha_{c0}. \tag{14}$$

The model proposed uses the shape parameter α_c to characterize the ductility of the material. Compared with the traditional statistical analysis indexes such as R^2 and

RMSE, the shape parameter α_c has more practical significance. A smaller α_c means a lower descending gradient and thus indicates better ductility of concrete. α_c was used to characterize the descending section in different studies including the GB50010-2010 model. α_{c0} is the shape factor for descending section from the GB50010-2010 model.

For RPRPC with steel fibers, steel fiber amount greatly influences the ductility of concrete. Four concrete models considering steel fibers (the Prabha model [49], Lv model [50], Ding model [51], and Lee model [52]) were selected (Fig. 10).

The Prabha model [49] was developed based on the Collins model with a modification of the parameter k to correlate with the steel fiber reinforcement index RI. For Group C, the Prabha model failed to predict the peak point of the curve correctly, and it also overestimated the ductility.

The Lv model was based on the GB50010-2010 model. Instead of RI, the L/D ratio and volume proportion of steel fiber are used as two variables, and α_c is modified. The Lv model had a steeper descending section for A4, and a smoother curve for C2 and C4 compared with the test curves.

The Ding model modified the GB50010-2010 model by using RI. The model made better prediction for concrete with high strength or high steel fiber proportion in this study, but it overestimated the ductility of concrete with relatively lower strength or lower steel fiber proportion.

The Lee model overestimated the ductility of RPRPC in general and could not include concrete without steel fiber due to the limitation of the equation form.

Based on the above analysis and the descending section model for RPRPC without steel fiber, the correction factor of steel fiber for the shape coefficient of the descending section α_c is proposed as Eq. (15). And α_c for RPRPC with steel fiber is proposed as Eq. (16).

$$\varphi_{sf} = -0.18V_{sf}^2 + 0.42V_{sf}, \tag{15}$$

$$\alpha_c = (\varphi_{rp} + \varphi_{sf})\alpha_{c0}. \tag{16}$$

The model curves can be compared with the descending section of the test curves, as shown in Fig. 10(e), and the accuracy is estimated in Table 6, showing that the model exhibits good accuracy. The predicted values of shape parameter $\alpha_c$are compared with values from the test curves, as shown in Fig. 12; the model curves agreed with the test curves very well.

Table 6 Accuracy of proposed model for descending section

Metric	A1	A2	A3	A4(C1)	C2	C4	Average
R^2	0.8705	0.9539	0.9633	0.8977	0.9431	0.9900	0.9364
RMSE	0.8172	4.0282	2.6080	1.9521	4.1974	1.8751	2.5797

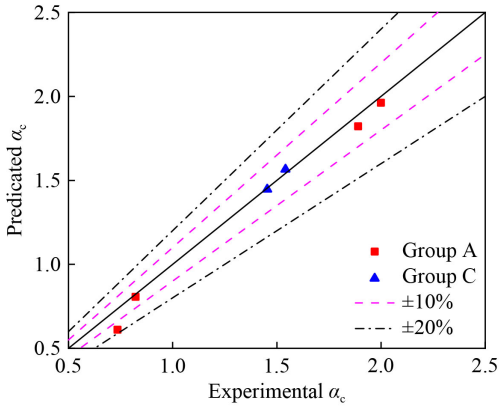

Fig. 12 Experimental and predicted results of shape parameters α_c.

5 Conclusions

A uniaxial compression constitutive model of RPRPC was developed and the following conclusions were drawn.

1) As the RP replacement ratio increased from 0% to 30%, the compressive strength and the elastic modulus of RPRPC decreased gradually.

2) With the rise in the amount of silica fume from 10% to 20%, the compressive strength of RPRPC increased significantly but the elastic modulus showed little decrease. With the increase of steel fiber content from 0% to 2%, the compressive strength and elastic modulus of RPRPC increased significantly.

3) When the RP replacement ratio increased from 0% to 10%, 20%, and 30%, the relative absorbed energy increased gradually, and relationship between RP replacement ratio and relative absorbed energy was close to linear. When the steel fiber content increased from 1% to 1.5% and 2%, the relative absorbed energy decreased gradually, and the compressive toughness index increased at first and then reduced slightly, indicating there is a upper limit for the proportion of steel fibers for increasing the energy absorption capacity.

4) The theoretical models of compressive strength, elastic modulus and relative absorbed energy for RPRPC with or without steel fibers were established. The models and experimental findings were in good agreement.

5) A model for a uniaxial compressive stress–strain curve of RPRPC was established, with the effects of the RP replacement ratio and the amount of steel fibers considered. The models and experimental findings were in good agreement.

6) In the future, other mechanical properties of RPRPC, such as tensile and flexural properties, should be studied, the mix proportions used in this experiment should be compared with those examined in other relevant studies to discover some rules regarding the mechanical properties of RPRPC.

Acknowledgements The research was supported by National Key R&D Program of China (No. 2022YFC3801100), the National Natural Science Foundation of China (Grant No. 51208373) and the Shanghai Pujiang Program (No. 12PJ1409000). The authors would like to thank Dr. Xiaodan Ren and Dr. Jiangtao Yu, professors of College of Civil Engineering in Tongji University, for their help in the experiment.

Competing interests The authors declare that they have no competing interests.

References

1. Larsen I L, Thorstensen R T. The influence of steel fibres on compressive and tensile strength of ultra high performance concrete: A review. Construction & Building Materials, 2020, 256: 119459
2. Sanjuan M A, Andrade C. Reactive powder concrete: Durability and applications. Applied Sciences, 2021, 11(12): 5629
3. Wu H, Zuo J, Zillante G, Wang J, Yuan H. Construction and demolition waste research: A bibliometric analysis. Architectural Science Review, 2019, 62(4): 354–365
4. Mao X Q, Qu W J, Zhu P. Recycled powder for construction waste: A review. China Concrete and Cement Products, 2015, 2015(8): 89–93 (in Chinese)
5. Zhu P, Mao X, Qu W. Investigation of recycled powder as supplementary cementitious material. Magazine of Concrete Research, 2019, 71(24): 1312–1324
6. Mao X, Qu W, Zhu P. Mixture optimization of green reactive powder concrete with recycled powder. Journal of Materials in Civil Engineering, 2019, 31(5): 04019033
7. Kwon E, Ahn J, Cho B, Park D. A study on development of recycled cement made from waste cementitious powder. Construction & Building Materials, 2015, 83: 174–180
8. Kim Y J, Choi Y W. Utilization of waste concrete powder as a substitution material for cement. Construction & Building Materials, 2012, 30: 500–504
9. Kim Y J. Quality properties of self-consolidating concrete mixed with waste concrete powder. Construction & Building Materials, 2017, 135: 177–185
10. Li L G, Lin Z H, Chen G M, Kwan A K H, Li Z H. Reutilization of clay brick waste in mortar: Paste replacement versus cement replacement. Journal of Materials in Civil Engineering, 2019, 31(7): 04019129
11. Xiao J, Ma Z, Sui T, Akbarnezhad A, Duan Z. Mechanical properties of concrete mixed with recycled powder produced from construction and demolition waste. Journal of Cleaner Production, 2018, 188: 720–731
12. Xue C, Shen A, Guo Y, He T. Utilization of construction waste composite powder materials as cementitious materials in small-scale prefabricated concrete. Advances in Materials Science and Engineering, 2016, 2016: 1–11
13. Tang Q, Ma Z, Wu H, Wang W. The utilization of eco-friendly recycled powder from concrete and brick waste in new concrete: A critical review. Cement and Concrete Composites, 2020, 114: 103807
14. Zhu P, Mao X, Qu W, Li Z, Ma Z J. Investigation of using recycled powder from waste of clay bricks and cement solids in reactive powder concrete. Construction & Building Materials, 2016, 113: 246–254
15. Graybeal B A. Compressive behavior of ultra-high-performance fiber-reinforced concrete. ACI Materials Journal, 2007, 104(2): 146–152
16. Bae B I, Choi H K, Lee B S, Bang C H. Compressive behavior and mechanical characteristics and their application to stress−strain relationship of steel fiber-reinforced reactive powder concrete. Advances in Materials Science and Engineering, 2016, 2016: 1–11
17. Collins M P, Mitchell D, Macgregor J G. Structural design considerations for high-strength concrete. Concrete International, 1993, 15(5): 27–34
18. Ji J, Kang W, Jiang L, Li Y, Ren H, Hao S, He L, Lin Y, Yu C. Mechanical behavior of reactive powder concrete made from local material subjected to axial pressure. Frontiers in Materials, 2021, 8: 737646
19. Zhang Y, Xin H, Correia J A F O. Fracture evaluation of ultra-high-performance fiber reinforced concrete (UHPFRC). Engineering Failure Analysis, 2021, 120: 105076
20. Hashim D T, Hejazi F, Lei V Y. Simplified constitutive and damage plasticity models for UHPFRC with different types of fiber. International Journal of Concrete Structures and Materials, 2020, 14(1): 45
21. Tang J Y, Ma W, Pang Y Y, Fan J C, Liu D X, Zhao L P, Sheikh S A. Uniaxial compression performance and stress−strain constitutive model of the aluminate cement-based UHPC after high temperature. Construction & Building Materials, 2021, 309: 125173
22. Wong C L, Mo K H, Yap S P, Alengaram U J, Ling T C. Potential use of brick waste as alternate concrete-making materials: A review. Journal of Cleaner Production, 2018, 195: 226–239
23. Ahmed S, Al-Dawood Z, Abed F, Mannan M A, Al-Samarai M. Impact of using different materials, curing regimes, and mixing procedures on compressive strength of reactive powder concrete—A review. Journal of Building Engineering, 2021, 44: 103238
24. Park J J, Ryu G S, Kang S T, Kim S W. The influence of the amount of silica fume on the mechanical property of ultra-high performance concrete. Key Engineering Materials, 2008, 385–387: 701–704
25. Wu Z, Shi C, He W, Wu L. Effects of steel fiber content and shape on mechanical properties of ultra high performance concrete. Construction & Building Materials, 2016, 103: 8–14
26. Ouyang X, Shi C, Wu Z, Li K, Shan B, Shi J. Experimental investigation and prediction of elastic modulus of ultra-high performance concrete (UHPC) based on its composition. Cement and Concrete Research, 2020, 138: 106241
27. Tang Z, Hu Y, Tam V W Y, Li W. Uniaxial compressive behaviors of fly ash/slag-based geopolymeric concrete with recycled aggregates. Cement and Concrete Composites, 2019, 104: 104
28. ASTM. Standard Test Method for Flexural Toughness and First-Crack Strength of Fiber Reinforced Concrete (Using Beam with Third-Point Loading), ASTM-C1018. West Conshohocken, PA: ASTM, 2006
29. CECS13. 89. Testing Method for Steel Fiber Reinforced Concrete.

Beijing: China Association for Engineering Construction Standardization, 1989 (in Chinese)
30. Letelier V, Tarela E, Moriconi G. Mechanical properties of concretes with recycled aggregates and waste brick powder as cement replacement. Procedia Engineering, 2017, 171: 627–632
31. Letelier V, Ortega J, Muñoz P, Tarela E, Moriconi G. Influence of waste brick powder in the mechanical properties of recycled aggregate concrete. Sustainability, 2018, 10(4): 1037
32. Liu Q, Li B, Xiao J, Singh A. Utilization potential of aerated concrete block powder and clay brick powder from C&D waste. Construction & Building Materials, 2020, 238: 117721
33. Quan H Z. Study on properties of self-compacting concrete with recycled powder. Advanced Materials Research, 2011, 250–253: 866–869
34. Lim J C, Ozbakkaloglu T. Stress–strain model for normal- and light-weight concretes under uniaxial and triaxial compression. Construction & Building Materials, 2014, 71: 492–509
35. Wu B, Liu C, Yang Y. Size effect on compressive behaviours of normal-strength concrete cubes made from demolished concrete blocks and fresh concrete. Magazine of Concrete Research, 2013, 65(19): 1155–1167
36. Wu B, Yu Y, Chen Z. Compressive behaviors of prisms made of demolished concrete lumps and fresh concrete. Applied Sciences, 2018, 8(5): 743
37. ASTM. Standard Test Method for Compressive Strength of Cylindrical Concrete Specimens. ASTM C39/39M-21. West Conshohocken, PA: ASTM, 2021
38. UNESCO. Reinforced Concrete: An International Manual. London: Butterworths, 1971
39. ACI 363R-10. Report on High-Strength Concrete. Michigan: American Concrete Institute, 2011
40. Alsalman A, Dang C N, Prinz G S, Hale W M. Evaluation of elastic modulus of ultra-high performance concrete. Construction & Building Materials, 2017, 153: 918–928
41. Guo X Y, Kang J F, Zhu J S. Constitutive relationship of ultrahigh performance concrete under uni-axial compression. Journal of Southwest University (Natural Science Edition), 2017, 47(2): 369–376 (in Chinese)
42. Carreira D J, Chu K H. Stress-strain relationship for plain concrete in compression. Journal of the American Concrete Institute, 1985, 82(6): 797–804
43. Guo Z H. Strength and Constitutive Model of Concrete: Principle and Application. Beijing: China Architecture & Building Press, 2004 (in Chinese)
44. Committee CEB. CEB-FIP Model Code 1990. Lausanne: Thomas Telford Ltd., 1993
45. GB50010-2010. Code for Design of Concrete Structures. Beijing: Ministry of Housing and Urban-Rural Development of the People's Republic of China, 2010 (in Chinese)
46. Ouyang X, Wu Z, Shan B, Chen Q, Shi C. A critical review on compressive behavior and empirical constitutive models of concrete. Construction & Building Materials, 2022, 323: 126572
47. Wu Y M. Study of the reactive powder concrete (RPC) about compressive stress-strain curve. Thesis for the Master's Degree. Guangzhou: Guangzhou University, 2012 (in Chinese)
48. Wee T H, Chin M S, Mansur M A. Stress−strain relationship of high-strength concrete in compression. Journal of Materials in Civil Engineering, 1996, 8(2): 70–76
49. Prabha S L, Dattatreya J, Neelamegam M. Stress strain behaviour of ultra high performance concrete under uniaxial compression. Int. J. Civ. Eng. Technol, 2014, 5: 187–194
50. Lv X L, Zhang Y, Nian X C. Experimental study on stress–strain curves for high-strength steel fiber reinforced concrete under monotonic and repeated compressive loadings. Journal of Building Structures, 2017, 38: 135–143 (in Chinese)
51. Ding X, Li C, Li Y, Lu Y, Song C, Zhao S. Experimental and numerical study on stress-strain behavior of self-compacting SFRC under uniaxial compression. Construction & Building Materials, 2018, 185: 30–38
52. Lee S C, Oh J H, Cho J Y. Compressive behavior of fiber-reinforced concrete with end-hooked steel fibers. Materials, 2015, 8(4): 1442–1458
53. Nematzadeh M, Salari A, Ghadami J, Naghipour M. Stress-strain behavior of freshly compressed concrete under axial compression with a practical equation. Construction & Building Materials, 2016, 115: 402–423
54. Wang P T, Shah S P, Naaman A E. Stress–strain curves of normal and lightweight concrete in compression. Journal of the American Concrete Institute, 1978, 75(11): 603–611